



OPEN

Artificial intelligence-based radiomics for the prediction of nodal metastasis in early-stage lung cancer

Yoshihisa Shimada^{1✉}, Yujin Kudo³, Sachio Maehara³, Kentaro Fukuta³, Ryuhei Masuno², Jinho Park² & Norihiko Ikeda³

We aimed to investigate the value of computed tomography (CT)-based radiomics with artificial intelligence (AI) in predicting pathological lymph node metastasis (pN) in patients with clinical stage 0–IA non-small cell lung cancer (c-stage 0–IA NSCLC). This study enrolled 720 patients who underwent complete surgical resection for c-stage 0–IA NSCLC, and were assigned to the derivation and validation cohorts. Using the AI software Beta Version (Fujifilm Corporation, Japan), 39 AI imaging factors, including 17 factors from the AI ground-glass nodule analysis and 22 radiomics features from nodule characterization analysis, were extracted to identify factors associated with pN. Multivariate analysis showed that clinical stage IA3 ($p = 0.028$), solid-part size ($p < 0.001$), and average solid CT value ($p = 0.033$) were independently associated with pN. The receiver operating characteristic analysis showed that the area under the curve and optimal cut-off values of the average solid CT value relevant to pN were 0.761 and -103 Hounsfield units, and the threshold provided sensitivity, specificity, and negative predictive values of 69%, 65%, and 94% in the entire cohort, respectively. Measuring the average solid-CT value of tumors for pN may have broad applications such as guiding individualized surgical approaches and postoperative treatment.

Abbreviations

AI	Artificial intelligence
AUC	Area under the curve
CI	Confidence interval
CT	Computed tomography
GGN	Ground-glass nodule
HR	Hazard ratio
HU	Hounsfield units
NPV	Negative predictive value
NSCLC	Non-small cell lung cancer
OS	Overall survival
PET	Positron emission tomography
RFS	Recurrence-free survival
ROC	Receiver-operating characteristics
SD	Standard deviation
3D	Three-dimensional

Pathological lymph node status is considered one of the most important prognostic factors in patients with early-stage non-small cell lung cancer (NSCLC)¹. There is an approximately 15–20% risk of occult lymph node metastasis in patients with stage I disease^{2–5}. The 5-year overall survival rates of patients with pathological N1, N2, and N3 NSCLC were 49%, 36%, and 20%, respectively¹. Given that pathological lymph node metastasis (pN) is a substantial threat to survival, identifying the relevant clinical factors is highly beneficial when considering

¹Department of Thoracic Surgery, Tokyo Medical University, 6-7-1 Nishishinjuku, Shinjuku-Ku, Tokyo 160-0023, Japan. ²Department of Radiology, Tokyo Medical University, Tokyo, Japan. ³Department of Thoracic Surgery, Tokyo Medical University, Tokyo, Japan. ✉email: zenkyu@za3.so-net.ne.jp

surgical approaches, the indication of adjuvant chemotherapies, optimal postoperative surveillance, and the prediction of prognostic outcomes in clinical stage IA NSCLC.

Various techniques, such as imaging and endoscopic modalities, have been reported to enable the stratification of patients with NSCLC according to their prognosis^{6–8}. Our recent report showed that quantitative computed tomography (CT) histogram analysis of lung tumors obtained by extracting voxel values enables the non-invasive prediction of pN in patients with clinical stage 0–IA NSCLC⁸. Cho et al. showed that radiological pure solid tumor and solid-part size were associated with pN1 and N2 lymph node metastases in patients with stage I NSCLC³. Furthermore, we conducted an artificial intelligence (AI) analysis of three-dimensional (3D) lung tumor imaging, showing that solid-part volume calculated using AI software was associated with an unfavorable prognosis in patients with radiologically solid-predominant NSCLC⁹.

Radiomics is a high-throughput quantitative tool that converts medical images into a large amount of pre-defined computational data. The potential application of radiomics in predicting lymph node metastasis, treatment response, and clinical outcomes of patients with lung cancer has recently attracted much attention^{10–14}. Radiomics-based approaches coupled with AI may serve as non-invasive and personalized decision support methods to identify prognostically high-risk cohorts with early-stage NSCLC. The purpose of our study was to evaluate CT-based radiomics analysis to preoperatively predict pN in patients with clinical stage 0–IA NSCLC.

Patients and methods

Patients. There were 1692 patients who underwent pulmonary resection for lung cancer between January 2008 and December 2015. The following exclusion criteria were applied: lung cancer other than NSCLC, clinical stage IB–IV, incomplete surgical resection, wedge resection, no mediastinal lymph node dissection, and pre-operative induction treatment. The remaining patients were those with clinical stage 0–IA NSCLC who underwent radical anatomical resection (lobectomy or segmentectomy) and systemic lymph node dissection at Tokyo Medical University Hospital. Among them, 233 patients were excluded because the AI imaging features of their lesions could not be processed. Low-fidelity CT images due to a limited number of CT slices and existing normal lung structures and non-malignant lesions resembling tumors cause the AI's misrecognition to a target tumor. Finally, 720 patients for whom AI processing using their chest CT was successfully performed were enrolled in this study. We randomly assigned 480 and 240 patients to the derivation and validation sets to balance the proportions of patients with pN, respectively. A consort diagram of patients included in the study was shown in Fig. 1. We reviewed the medical records of each patient for preoperative clinical information including TNM stage. The TNM stage was determined according to the eighth edition of the TNM classification of malignant tumors. The comorbidities included diabetes mellitus, cardiovascular disease, chronic obstructive pulmonary disease, cerebral disease, autoimmune disease, interstitial pneumonia, and asthma.

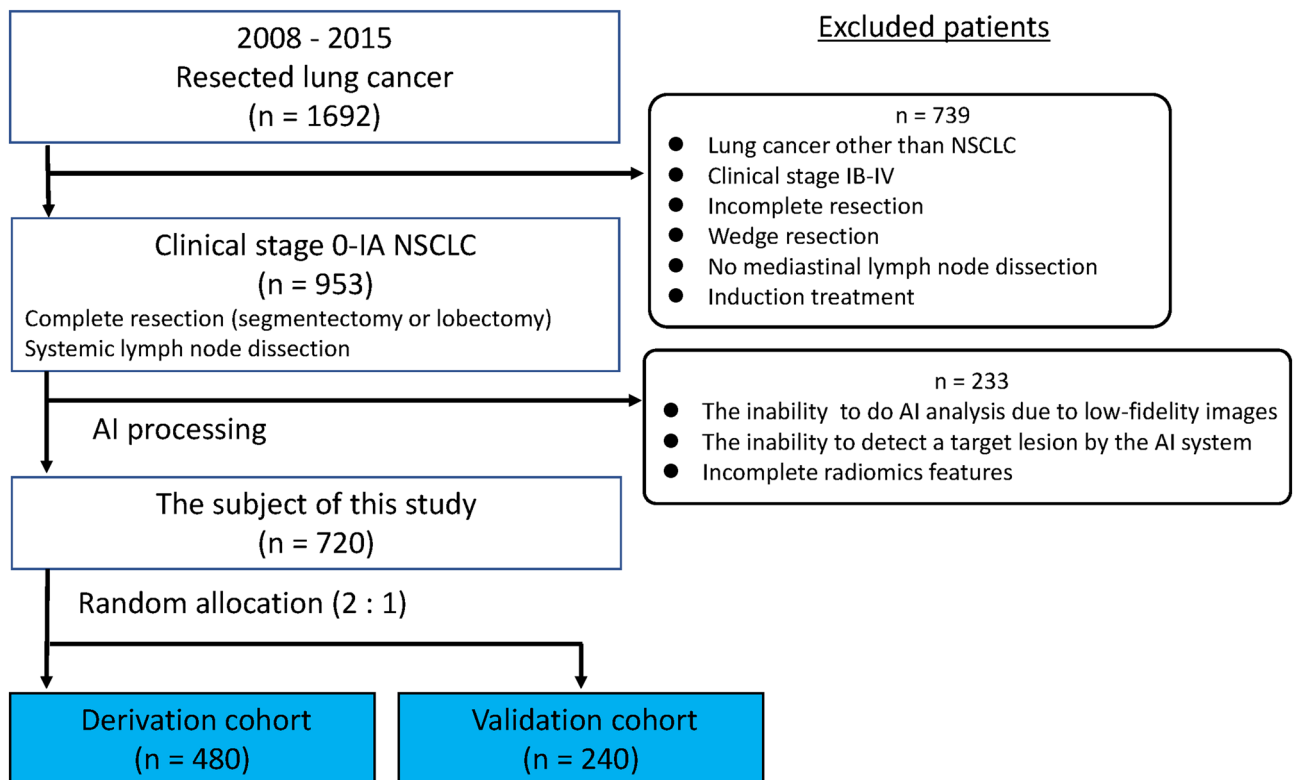


Figure 1. Consort diagram of patients included in the study. NSCLC—non-small cell lung cancer; ND—node dissection; AI—artificial intelligence.

Patient follow-up. Patients were examined at the 6-month intervals for the first 2 years and 1-year intervals on an outpatient basis, with the aim of continuing follow-up for 10 years after resection. Follow-up evaluations included physical examinations, chest radiography, and blood tests. Chest and abdominal CT scans were performed every 6 months in the first 2 years and annually from the third year. Further evaluations, including brain magnetic resonance imaging and bone scintigraphy, were performed when the symptoms or signs of recurrence were observed. Positron emission tomography/computed tomography (PET/CT) was performed when appropriate. The date of recurrence was defined as the date of histologic proof or the date of identification based on clinicoradiologic findings by a physician.

Radiological evaluation of primary tumor. All patients in this study underwent preoperative high-resolution CT and three-dimensional CT lung modeling. Helical CT images (1.25-mm-thick) were obtained from the whole lung. The whole tumor and solid-part sizes were preoperatively measured by two experienced thoracic radiologists (Dr. R.M. with 14 years and Dr. J.P. with 30 years of experience in chest CT interpretation, respectively). The solid-part size was defined as the maximum diameter of the solid component of the lung window, excluding the ground-glass nodules.

Radiomics and AI imaging analysis of CT images. After the lung CT Digital Imaging and Communications in Medicine (DICOM) format data were transmitted to the Synapse Vincent system (Fujifilm Corporation, Tokyo, Japan), the AI software Beta Version (AI software; Fujifilm Corporation) in the system automatically detected and segmented lung nodules in the bilateral lungs and reconstructed the 3D images of the lungs and nodules. This segmentation algorithm was based on the 3D-Convolutional Neural Network using a modified U-Net architecture. The network consisted of 17 convolutional layers. The system separated the solid-part of lung nodules from non-solid-parts (ground-glass nodules; [GGNs]), and determined the size, volume, and ratio of solid-part, non-solid-part, and whole tumor lesions, as well as CT histogram features. The total of 39 AI imaging features included 22 radiomics features and 17 features from the GGN analysis (Supplemental Table 1), and the radiomics features were automatically extracted and displayed as a score from 0 to 1 using a feature analysis function. The 22 radiomics features were based on the labeling of 5118 tumors, and the datasets of the developmental process were divided into training, validation, and test sets. The trained model gave a mean area under the curve (AUC) score of 0.93 for all features on the test dataset based on the information of radiological and histological diagnoses of tumor and non-tumor lesions (data not shown). This AI lung nodule analysis model uses a convolutional neural network based on VGG-16 and consists of 12 layers of convolution, with four layers removed from the output side of the VGG-16. To extract 3D radiomics features, 3D convolution was used for all the convolution layers. The 3D software automatically generated the 17 features from the GGN analysis. The software determined the volumes of the GGNs, radiologically solid lesions and whole tumor lesions, the ratios of GGNs or the radiologically solid lesions, and CT histograms data by the feature analysis function.

Statistical analysis. Overall survival (OS) was measured from the day of surgery to the day of death from any cause or the day on which the patient was last known to be alive. Recurrence-free survival (RFS) was measured as the interval between the date of surgery and date of recurrence, date of death from any cause, or date the patient was last known to be alive. OS and RFS curves were plotted using the Kaplan–Meier method, and differences in variables were determined using the log-rank test. Univariate and multivariate logistic regression analyses were performed to identify the factors associated with pN using a Cox proportional hazards model. A backward stepwise selection method was used to build logistic regression models, and variables with a threshold of $p < 0.15$ were adopted for the stepwise model selection procedure to prevent overlooking relevant factors. We conducted univariate and multivariate analyses separately using the 39 AI imaging features and other clinical factors. Pearson's chi-square test (for categorical data) and Student's *t* test (for continuous data) were used to compare two groups of data. Receiver operating characteristics (ROC) curves for lymph node metastasis and early recurrence were constructed, and the optimal cut-off values were determined using the AUC. All tests were two-sided, and statistical significance was set at $p < 0.05$. The SPSS statistical software package (version 28.0, DDR3 RDIMM; SPSS Inc., Chicago, IL, USA) was used for statistical analysis. Violin plots were constructed using the R package (version 4.0.5).

Ethical statement. The authors are accountable for all aspects of the work in ensuring that questions related to the accuracy or integrity of any part of the work are appropriately investigated and resolved. All procedures performed in this study involving human participants were performed in accordance with the Declaration of Helsinki (as reserved in 2013). The study was approved by the institutional review board of Tokyo Medical University (SH3951). Informed consent for the use and analysis of clinical data was obtained preoperatively for each patient.

Results

Patient characteristics are shown in Table 1. The derivation cohort included 236 men (49%) and 244 women (51%), while the validation cohort included 122 men (51%) and 118 women (49%). There were no significant differences between the two cohorts, except for surgical procedures. Segmentectomy was performed in 50 patients (10%) in the derivation cohort and in 11 patients (5%) in the validation cohort ($p = 0.008$).

Fifty-six patients (12%) in the derivation cohort and 27 patients (11%) in the validation cohort were found to have positive lymph nodes. Kaplan–Meier curves showed that pN status was significantly associated with OS and RFS in the derivation cohort (5-year OS rate 92.4% vs. 63.8%, $p < 0.001$, Fig. 2A; and 5-year RFS rate 84.5% vs. 40.1%, $p < 0.001$, Fig. 2B), the validation cohort (5-year OS rate 92.3% vs. 63.8%, $p < 0.001$, Fig. 2C; and 5-year

Variable	Derivation cohort <i>n</i> = 480 (%)	Validation cohort <i>n</i> = 240 (%)	<i>p</i> value
Age, years (mean ± SD)	23–86 (66 ± 10)	38–87 (67 ± 10)	0.245
Sex, male	236 (49)	122 (51)	0.673
Any smoking history	271 (57)	146 (61)	0.262
Comorbidities, present	227 (47)	132 (55)	0.051
FEV _{1.0} L (mean ± SD)	0.98–4.93 (2.36 ± 0.67)	0.89–4.93 (2.28 ± 0.64)	0.125
FEV _{1.0} % (mean ± SD)	39–96 (73 ± 9)	35–93 (73 ± 10)	0.795
Clinical stage			
0	32 (7)	13 (6)	(0-IA2 vs. IA3) 0.163
IA1	94 (20)	43 (18)	
IA2	201 (42)	95 (40)	
IA3	153 (32)	89 (37)	
Pathological stage			
IA	312 (65)	164 (68)	(I vs. II-III) 0.234
IB	92 (19)	46 (19)	
II	40 (8)	16 (7)	
III	36 (8)	14 (6)	
Histology			
Adenocarcinoma	422 (88)	204 (85)	0.274
Others	58 (12)	36 (15)	
Pathological lymph-node status			
N0	420 (88)	213 (89)	(N0 vs. N1-3) 0.869
N1	25 (5)	13 (5)	
N2	31 (7)	14 (6)	
N3	4 (1)	0	
Surgical procedure			
Lobectomy	430 (90)	229 (95)	0.008
Segmentectomy	50 (10)	11 (5)	

Table 1. Patient characteristics. *SD* standard deviation; *FEV* forced expiratory volume.

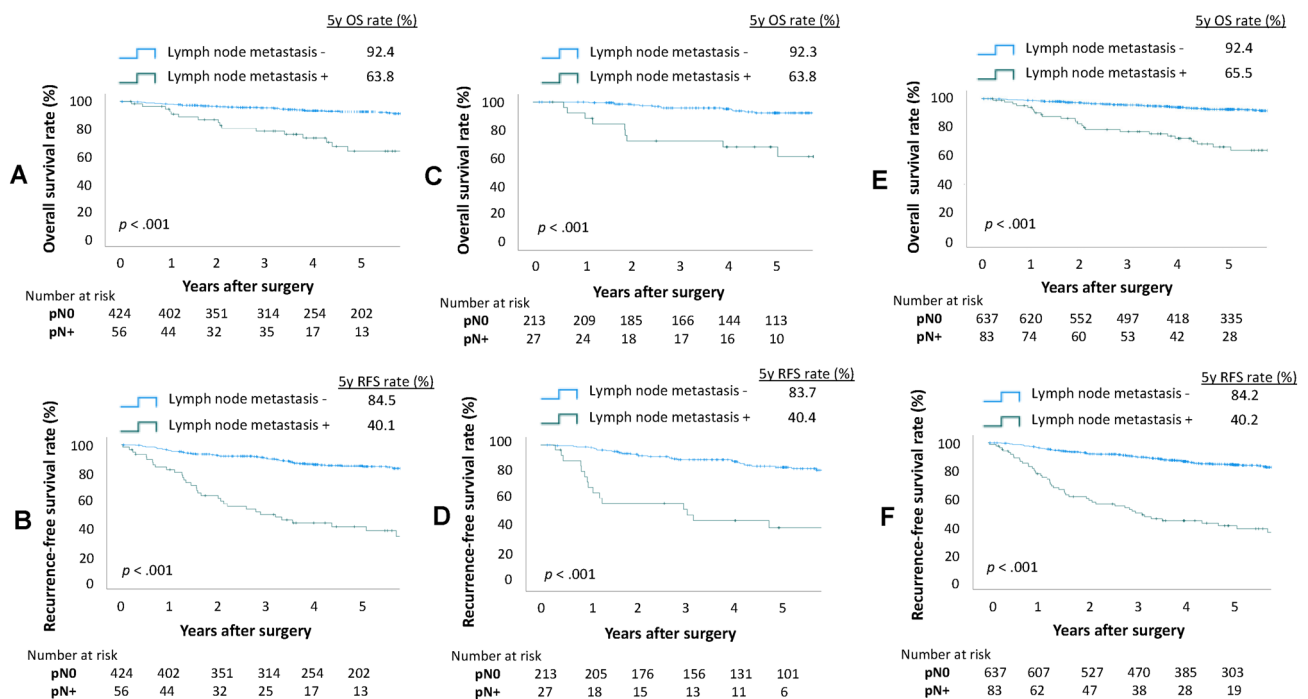


Figure 2. Overall survival and recurrence-free survival of clinical stage 0–IA patients according to status of lymph node metastasis status. (A) Overall survival and (B) recurrence-free survival of patients in the derivation cohort. (C) Overall survival and (D) recurrence-free survival of patients in the validation cohort. (E) Overall survival and (F) recurrence-free survival of patients in the entire cohort. pN0—pathological lymph node negative; pN+—pathological lymph node positive.

RFS rate 83.7% vs. 40.4%, $p < 0.001$, Fig. 2D), and in the entire cohort (5-year OS rate 92.4% vs. 65.5%, $p < 0.001$, Fig. 2E; and 5-year RFS rate 84.2% vs. 40.2%, $p < 0.001$, Fig. 2F).

The p -value significance of the correlations between the 39 AI imaging features and the pN is shown in Fig. 3, and 17 factors were found to be significant in both cohorts. Univariate analyses of RFS in the derivation using clinical factors such as age, sex, smoking habit (presence versus absence), FEV1.0%, comorbidities (presence versus absence), solid-part size, clinical stage (0–IA2 versus IA3), and surgical procedure (lobectomy versus segmentectomy) showed that larger solid-part size (hazard ratio [HR] 2.82, 95% confidence interval (CI) 1.98–4.02, $p < 0.001$) and clinical stage IA3 (HR 2.36, 95%CI 1.49–3.76, $p < 0.001$) were found to be significant unfavorable RFS factors (Table 2). Solid-part size (HR 7.96, 95%CI 3.26–19.48, $p < 0.001$) and clinical stage IA3 (HR 3.23, 95%CI 1.13–9.19, $p = 0.028$) were also independently associated with poor RFS on multivariate analysis (Table 2). Among the AI imaging features, the average solid CT value (HR 1.01, 95%CI 1.00–1.02, $p = 0.033$) was the only independent factor associated with unfavorable RFS on multivariate analysis (Table 2).

To investigate the effect of the statistically significant predictive factors, solid-part size, and average solid CT value on pN, we calculated ROC curves in the derivation cohort (Supplementary Figure. 1). The AUC and optimal cut-off values relevant to pN were 0.754 and 1.83 cm for solid-part size and 0.761 and –103 Hounsfield units (HU) for the average solid CT value.

Violin plots were constructed to visualize the comparative distributions of the solid-part size of the validation (Fig. 4A) and the entire cohort (Fig. 4B), and the average solid CT value of the validation (Fig. 4C) and the entire cohort (Fig. 4D) to analyze the association with pN. Significant differences were observed in the solid-part size in the validation ($p = 0.021$) and the entire cohort ($p < 0.001$), and in the average solid CT value in the validation ($p < 0.001$) and entire cohort ($p < 0.001$). Patients in the derivation, validation, and entire cohorts were dichotomized at 1.83 cm of solid-part size, which showed pN ratios of 23% and 4% ($p < 0.001$), 15% and 8% ($p = 0.114$), and 20% and 6% ($p < 0.001$) for the high- and low-risk cohorts, respectively. Those in the derivation, validation and entire cohorts were dichotomized at –103 HU of the average solid CT value, showing a pN ratio of 22% and 6% ($p < 0.001$), 17% and 7% ($p = 0.011$), and 20% and 6% ($p < 0.001$) for the high and low-risk cohorts, respectively (Table 3). The threshold provided sensitivities of 70%, 67%, and 69%, specificities of 68%,

	Derivation	Validation	Significant p -value		Derivation	Validation	Significant p -value
Clear boundary	0.000	0.002		Analyzed volume	0.166	0.267	
Irregular shape	0.002	0.415		GGN volume	0.098	0.956	
Round shape	0.001	0.626		GGN ratio	0.000	0.000	
Smooth shape	0.437	0.000		Solid volume	0.000	0.001	
Irregular edge	0.568	0.583		Solid ratio	0.000	0.000	
Serrated edge	0.000	0.011		Solid area	0.000	0.001	
Spicula	0.000	0.192		Area	0.22	0.201	
Lobulated edge	0.000	0.006		Max. solid length	0.000	0.005	
Polygon edge	0.042	0.002		Max. length	0.15	0.277	
Bronchus translucency	0.002	0.07		Average solid CT value	0.000	0.005	
Cavity	0.203	0.253		Average CT value	0.000	0.000	
Pleural indentation	0.187	0.194		Average solid CT value SD	0.000	0.006	
Pleural contact	0.764	0.662		CT value SD	0.273	0.196	
Solid	0.000	0.000		Max. solid CT value	0.000	0.071	
Part solid	0.002	0.009		Max. CT value	0.000	0.072	
GGO	0.000	0.000		Min. solid CT value	0.000	0.013	
Calcification	0.027	0.849		Min. CT value	0.000	0.134	
Fatness	0.732	0.884					
Bronchial convergence	0.227	0.351					
Bronchial compression	0.354	0.033					
Pleural recess	0.101	0.333					
Pleural hypertrophy	0.481	0.729					

Both p -value < .05
 p -value < .05 in derivation
 p -value < .05 in validation
 Not significant

Figure 3. Heat map showing the p -value significance of correlations between the 39-feature signatures and pathological lymph node metastasis. Artificial intelligence imaging analysis indicates the signatures related to lymph node metastasis in the derivation and validation cohorts.

Factors among clinicopathological factors	Univariate analysis	
	Hazard ratio (95% CI)	<i>p</i> value
Age	1.02 (1.00–1.04)	0.086
Sex (male vs. female)	1.45 (0.91–2.30)	0.118
Smoking	1.20 (0.78–1.86)	0.407
FEV _{1.0} %	0.77 (0.55–1.07)	0.122
Comorbidities	1.36 (0.86–2.16)	0.191
Solid-part size	2.82 (1.98–4.02)	<0.001
Clinical stage (IA3 vs. 0-IA2)	2.36 (1.49–3.76)	<0.001
Procedure (lobectomy vs. segmentectomy)	2.67 (0.82–8.73)	0.104
Factors among clinicopathological factors	Multivariate analysis	
	Hazard ratio (95% CI)	<i>p</i> value
Solid-part size	7.96 (3.26–19.48)	<0.001
Clinical stage (IA3 vs. 0-IA2)	3.23 (1.13–9.19)	0.028
Procedure (lobectomy vs. segmentectomy)	3.34 (0.43–25.65)	0.247
Factors among AI imaging features	Multivariate analysis	
	Hazard ratio (95% CI)	<i>p</i> value
Average solid CT value	1.01 (1.00–1.02)	0.033
Maximum solid CT value	1.00 (1.00–1.01)	0.084
Bronchus translucency	3.10 (0.80–1.90)	0.101

Table 2. Univariate and multivariate analyses of lymph node metastasis in the derivation cohort. CI confidence interval; FEV forced expiratory volume; AI artificial intelligence; CT computed tomography.

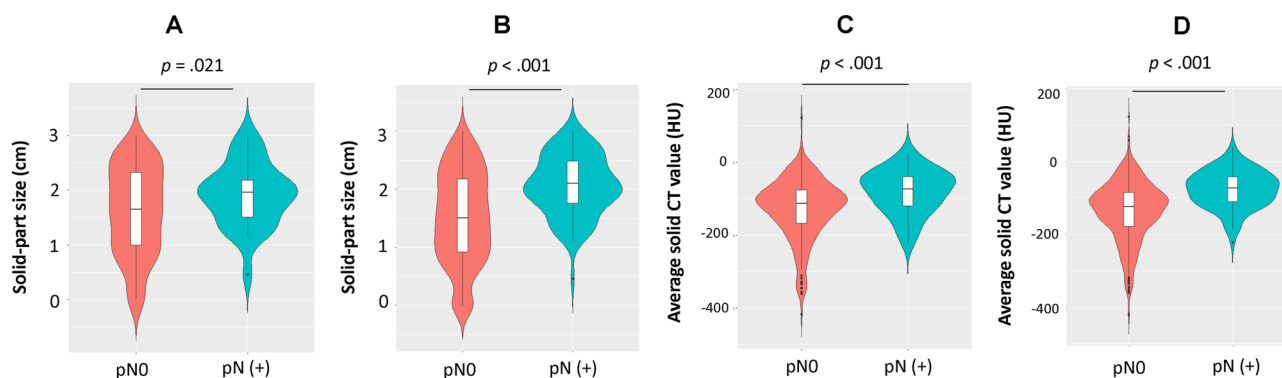


Figure 4. Violin plots for the comparison of the distribution of solid-part size in the validation cohort (A) and entire cohort (B), and average solid CT value in the artificial intelligence in the validation cohort (C) and entire cohort (D). pN(+)—pathological lymph node positive; CT—computed tomography; HU—Hounsfield units.

59%, and 65%, and negative predictive values of 94%, 93%, and 94% in the derivation, validation, and entire cohorts, respectively (Table 3).

Discussion

In the present study, we found that the average solid-CT value of the tumor extracted from the AI imaging analysis as well as the clinical stage and the solid-part size of the tumor, were independently associated with pN in patients with clinical stage 0-IA NSCLC. The AUC of the average solid CT value for pN was 0.761, and the cut-off level was -103 HU, which is a better threshold associated with pN than a solid-part size on chest CT based on the results of the pN ratio and accuracy.

Preoperative identification of the boundary between high- and low-risk populations on the pN is crucial for optimal surgical procedures, particularly in clinical stage I NSCLC^{3,5,8,15}. Cho et al. showed that higher clinical stage and larger solid tumor size were associated with pN, consistent with our results³. Koike et al. identified four significant predictive factors including CTR for pN in patients with stage IA NSCLC⁴. Their patients were dichotomized at 0.89 of CTR, which showed a sensitivity of 98%, specificity of 43% and accuracy of 47%, respectively⁴. Kaseda et al. demonstrated that the SUVmax of the tumor was independently associated with occult lymph node metastasis in patients with stage I NSCLC, and the thresholds of the SUVmax provided a sensitivity of 68%, specificity of 53% and accuracy of 55%, respectively¹⁵. Even though those studies showed higher sensitivities for pN, lower specificities ultimately led to lower accuracies than our results. We recently showed that

Cohort	Solid-part size	pN (%)	<i>p</i> value	Sensitivity (%)	Specificity (%)	Accuracy (%)	NPV (%)
Derivation	> 1.83 cm	44 (23)	< 0.001	44/56 (79)	278/424 (66)	322/480 (67)	278/290 (96)
	≤ 1.83 cm	12 (4)					
Validation	> 1.83 cm	16 (15)	0.114	16/27 (59)	121/213 (57)	137/240 (57)	121/132 (92)
	≤ 1.83 cm	11 (8)					
All	> 1.83 cm	60 (20)	< 0.001	60/83 (72)	399/637 (63)	459/720 (64)	399/422 (95)
	≤ 1.83 cm	23 (6)					
Cohort	Average solid CT value	pN (%)	<i>p</i> value	Sensitivity (%)	Specificity (%)	Accuracy (%)	NPV (%)
Derivation	> - 103 HU	39 (22)	< 0.001	39/56 (70)	288/424 (68)	327/480 (68)	288/305 (94)
	≤ - 103 HU	17 (6)					
Validation	> - 103 HU	18 (17)	0.011	18/27 (67)	126/213 (59)	144/240 (60)	126/135 (93)
	≤ - 103 HU	9 (7)					
All	> - 103 HU	57 (20)	< 0.001	57/83 (69)	414/637 (65)	471/720 (65)	414/440 (94)
	≤ - 103 HU	26 (6)					

Table 3. Correlation between the significant values and lymph node metastasis. *pN* pathological lymph node metastasis; *NPV* negative predictive value; *CT* computed tomography; *HU* Hounsfield units.

quantitative CT histogram analysis of lung tumors contributed to the noninvasive prediction of pN in patients with clinical stage IA NSCLC⁸. Average solid CT value obtained in the current study is one of the CT histogram parameters, and growing evidence suggests that quantitative CT histogram analysis of lung cancer is helpful in detecting imaging variables associated with postoperative outcomes and histologic invasiveness^{16–19}. Numerous other studies have reported factors associated with pN, such as age, histology, maximum standardized uptake values on PET/CT, solid-part size, and the maximum consolidation diameter to the maximum tumor diameter (CTR) in early-stage NSCLC^{20–23}. The ratio of CTR and solid-part size seen on HRCT has a greater chance of identified a pathological invasive component^{21,24}. Patients with a larger proportion of solid-part size had a higher recurrence rate regardless of surgical procedures^{24,25}. The present study demonstrated that the solid-part size was significantly associated with pN. HRCT plays a vital role in the diagnosis, and clinical decision making, and predicting patient outcomes in early-stage NSCLC. However, it is important to note that lung lesions with an irregularly shaped solid-part in the greatest dimension sometimes cause inter- and intra-observer variability.

Several studies have reported that radiomics approaches were highly useful for predicting pN in patients with NSCLC^{13,26,27}. Cong et al. established a radiomics model in predicting pN in early-stage NSCLC, and the predictive performance of their radiomics model was significantly better than that of clinical factor-based model¹³. Radiomics implementation comprises several processes, such as imaging, feature extraction, feature selection, signature building, and analysis. Usually, the region of interest on CT images is manually outlined by experienced radiologists. By contrast, the current radiomics analysis demonstrated that 39 AI imaging features could be automatically extracted and displayed as measures and scores. We believe that our work may serve as a promising method for predicting pN in a non-invasive manner, allowing physicians without technical expertise in the context of image synthesis to easily conduct AI analysis to unravel tumor phenotypic characteristics.

This study has several limitations. First, it was a retrospective review of patients from a single institution, and inherent biases existed. Second, not all preoperative CT images from patients were successfully processed using our radiomics analysis. There were cases in which a radiomics signature could not be obtained because of low-fidelity CT images and target lesions unrecognized by the AI system. Third, our study only used CT imaging features. PET/CT is highly useful for predicting prognosis and detecting pathological invasive factors, including lymph node metastasis, even though there are various causes of false-positive and false-negative results^{6,23}. However, 49% of patients were assessed using the same PET/CT setting, whereas the remaining were assessed by other scanners or had no PET/CT examinations in this study (data not shown). Therefore, we excluded data derived from PET/CT from the analyses. Fourth, the AI used in this study was specific to the software package used by our group. Applying these results to other centers would require the use of the same software. Therefore, external validation of this study outside our center could not be performed currently. Finally, the cut-off values from the ROC curves, such as - 103 HU on the average solid CT value and 1.83 cm on the solid-part size for pN were arbitrary. Hence, the results can vary depending on the number of patients or type of CT scanning protocol used although we performed the validation analyses to see if these thresholds were useful to predict pN.

In conclusion, AI software in CT-based radiomics provides significant imaging features for the prediction of pN in patients with clinical stage 0–IA NSCLC. Measuring the average solid CT value of tumors for pN may have broad clinical applications such as guiding surgical approaches and individualized postoperative treatment.

Data availability

The analyzed data in this article will be shared on reasonable request to the corresponding author, except for the deviation and validation dataset for the radiomics analysis by AI software.

Received: 17 September 2022; Accepted: 16 January 2023

Published online: 19 January 2023

References

- Asamura, H. *et al.* The international association for the study of lung cancer lung cancer staging project: Proposals for the revision of the N descriptors in the forthcoming 8th edition of the TNM classification for lung cancer. *J. Thorac. Oncol.* **10**, 1675–84 (2015).
- Asamura, H. *et al.* Lymph node involvement, recurrence, and prognosis in resected small, peripheral, non-small-cell lung carcinomas: Are these carcinomas candidates for video-assisted lobectomy?. *J. Thorac. Cardiovasc. Surg.* **111**, 1125–1134 (1996).
- Cho, S. *et al.* Predictive factors for node metastasis in patients with clinical stage I non-small cell lung cancer. *Ann. Thorac. Surg.* **96**, 239–245 (2013).
- Koike, T. *et al.* Predictive risk factors for mediastinal lymph node metastasis in clinical stage IA non-small-cell lung cancer patients. *J. Thorac. Oncol.* **7**, 1246–1251 (2012).
- Li, L. *et al.* Risk factors for predicting the occult nodal metastasis in T1–2N0M0 NSCLC patients staged by PET/CT: Potential value in the clinic. *Lung Cancer* **81**, 213–217 (2013).
- Schmidt-Hansen, M. *et al.* PET-CT for assessing mediastinal lymph node involvement in patients with suspected resectable non-small cell lung cancer. *Cochrane Database Syst. Rev.* **11**, CD009519 (2014).
- Vial, M. R. *et al.* Diagnostic performance of endobronchial ultrasound-guided mediastinal lymph node sampling in early stage non-small cell lung cancer: A prospective study. *Respirology* **23**, 76–81 (2018).
- Shimada, Y. *et al.* Computed tomography histogram approach to predict lymph node metastasis in patients with clinical stage IA lung cancer. *Ann. Thorac. Surg.* **108**(4), 1021–8. <https://doi.org/10.1016/j.athoracsur.2019.04.082> (2019).
- Kudo, Y. *et al.* Artificial intelligence analysis of three-dimensional imaging data derives factors associated with postoperative recurrence in patients with radiologically solid-predominant small-sized lung cancers. *Eur. J. Cardiothorac. Surg.* **61**, 751–760 (2022).
- Colen, R. R. *et al.* Radiomics analysis for predicting pembrolizumab response in patients with advanced rare cancers. *J. Immunother. Cancer* **9**, e001752 (2021).
- Wang, T. *et al.* Radiomics signature predicts the recurrence-free survival in stage I non-small cell lung cancer. *Ann. Thorac. Surg.* **109**, 1741–1749 (2020).
- Sun, Y. *et al.* Radiomics for lung adenocarcinoma manifesting as pure ground-glass nodules: Invasive prediction. *Eur. Radiol.* **30**, 3650–3659 (2020).
- Cong, M. *et al.* Development of a predictive radiomics model for lymph node metastases in pre-surgical CT-based stage IA non-small cell lung cancer. *Lung Cancer* **139**, 73–79 (2020).
- Chen, D. *et al.* Radiomics-based prediction for tumour spread through air spaces in stage I lung adenocarcinoma using machine learning. *Eur. J. Cardiothorac. Surg.* **58**, 51–58 (2020).
- Kaseda, K. *et al.* Risk factors for predicting occult lymph node metastasis in patients with clinical stage I non-small cell lung cancer staged by integrated fluorodeoxyglucose positron emission tomography/computed tomography. *World J. Surg.* **40**, 2976–2983 (2016).
- Son, J. Y. *et al.* Quantitative CT analysis of pulmonary ground-glass opacity nodules for the distinction of invasive adenocarcinoma from pre-invasive or minimally invasive adenocarcinoma. *PLoS ONE* **9**, e104066 (2014).
- Eriguchi, D. *et al.* Predictive accuracy of lepidic growth subtypes in early-stage adenocarcinoma of the lung by quantitative CT histogram and FDG-PET. *Lung Cancer* **125**, 14–21 (2018).
- Bak, S. H. *et al.* Quantitative CT scanning analysis of pure ground-glass opacity nodules predicts further CT scanning change. *Chest* **149**, 180–91 (2016).
- Tsuchiya, N., Doai, M., Usuda, K., Uramoto, H. & Tonami, H. Non-small cell lung cancer: Whole-lesion histogram analysis of the apparent diffusion coefficient for assessment of tumor grade, lymphovascular invasion and pleural invasion. *PLoS ONE* **12**, e0172433 (2017).
- Hattori, A. *et al.* Radiological classification of multiple lung cancers and the prognostic impact based on the presence of a ground glass opacity component on thin-section computed tomography. *Lung Cancer* **113**, 7–13 (2017).
- Hattori, A. *et al.* Prognostic impact of a ground glass opacity component in the clinical T classification of non-small cell lung cancer. *J. Thorac. Cardiovasc. Surg.* **154**, 2102–2110 (2017).
- Furumoto, H. *et al.* Prognostic impact of the integration of volumetric quantification of the solid part of the tumor on 3DCT and FDG-PET imaging in clinical stage IA adenocarcinoma of the lung. *Lung Cancer* **121**, 91–96 (2018).
- Kaira, K. *et al.* Biological significance of 18F-FDG uptake on PET in patients with non-small-cell lung cancer. *Lung Cancer* **83**, 197–204 (2014).
- Hattori, A. *et al.* Importance of ground glass opacity component in clinical stage IA radiologic invasive lung cancer. *Ann. Thorac. Surg.* **104**, 313–320 (2017).
- Hattori, A. *et al.* Neither maximum tumor size nor solid component size is prognostic in part-solid lung cancer: Impact of tumor size should be applied exclusively to solid lung cancer. *Ann. Thorac. Surg.* **102**, 407–415 (2016).
- Yang, X. *et al.* A new approach to predict lymph node metastasis in solid lung adenocarcinoma: A radiomics nomogram. *J. Thorac. Dis.* **10**(Suppl 7), S807–S819 (2018).
- Zhong, Y. *et al.* Radiomics approach to prediction of occult mediastinal lymph node metastasis of lung adenocarcinoma. *AJR Am. J. Roentgenol.* **211**, 109–113 (2018).

Acknowledgements

We would like to thank Editage (www.editage.com) for the English language editing. We also thank Mami Murakami for assistance with the statistical analyses.

Author contributions

Conception and design: S.Y. Administrative support: I.N. Provision of study materials of patients: S.Y. Collection and assembly of data: S.Y., K.Y., M.S., F.K. Data analysis and interpretation: S.Y., M.R., P.J. Manuscript writing: All authors. Final approval of manuscript: All authors.

Funding

Norihiko Ikeda reports a research grant to the Department of Surgery, Tokyo Medical University, from the Fujifilm Corporation.

Competing interests

Dr. Shimada, Dr. Kudo, Dr. Maehara, Dr. Masuno, Dr. Fukuta, and Dr. Park have no conflicts to disclose. Dr. Ikeda reports grants and personal fees from AstraZeneca, grants and personal fees from Boehringer Ingelheim, grants and personal fees from Chugai Pharma, grants and personal fees from Eli Lilly, grants and personal fees from MSD, grants and personal fees from Nihon Medi-Physics, grants and personal fees from Ono Pharmaceutical,

grants and personal fees from Pfizer, grants and personal fees from Taiho Pharmaceutical, grants and personal fees from Teijin, and personal fees from Bristol-Meyers Squibb Japan outside the submitted work.

Additional information

Supplementary Information The online version contains supplementary material available at <https://doi.org/10.1038/s41598-023-28242-7>.

Correspondence and requests for materials should be addressed to Y.S.

Reprints and permissions information is available at www.nature.com/reprints.

Publisher's note Springer Nature remains neutral with regard to jurisdictional claims in published maps and institutional affiliations.



Open Access This article is licensed under a Creative Commons Attribution 4.0 International License, which permits use, sharing, adaptation, distribution and reproduction in any medium or format, as long as you give appropriate credit to the original author(s) and the source, provide a link to the Creative Commons licence, and indicate if changes were made. The images or other third party material in this article are included in the article's Creative Commons licence, unless indicated otherwise in a credit line to the material. If material is not included in the article's Creative Commons licence and your intended use is not permitted by statutory regulation or exceeds the permitted use, you will need to obtain permission directly from the copyright holder. To view a copy of this licence, visit <http://creativecommons.org/licenses/by/4.0/>.

© The Author(s) 2023